

Cite this: *J. Mater. Chem. A*, 2019, 7, 19668Received 22nd June 2019
Accepted 29th July 2019

DOI: 10.1039/c9ta06734e

rsc.li/materials-a

Metal-free energy storage systems: combining batteries with capacitors based on a methylene blue functionalized graphene cathode†

Yadi Zhang,^{ab} Yufeng An,^a Langyuan Wu,^a Heng Chen,^a Zihan Li,^a Hui Dou,^{id a} Vignesh Murugadoss,^{bcd} Jincheng Fan,^{be} Xiaogang Zhang,^{id *a} Xianmin Mai^{†f} and Zhanhu Guo^{id *b}

Beyond conventional hybrid ion capacitors (HICs) based on porous carbon capacitive materials, the introduction of faradaic pseudocapacitance in HICs is an effective method to enhance energy density. Herein, we prepare methylene blue functionalized graphene (MB-X) composites taking advantage of electrostatic and extensive π -conjugated interaction. The test results confirm that the composites have high rate capability and excellent cycle stability on account of the synergistic effect between graphene and MB molecules. In order to improve the safety of HICs, an aqueous electrolyte is a promising candidate as long as the cell voltage can be efficiently increased. Therefore, we skillfully employ aqueous solutions with different pH values as asymmetric electrolytes to assemble HICs, where polyimide acts as the battery material and MB-X serves as the capacitive material. Thanks to the asymmetric electrolytes, the constructed aqueous HICs can operate at a cell voltage of 1.9 V, much larger than the decomposition voltage of water. Moreover, the flexible structure, and reversible and fast redox reactions of both the anode and cathode make the aqueous HICs display a maximum energy density of 48.6 W h kg⁻¹ and a maximum power density of 19 kW kg⁻¹, as well as a long-cycle lifetime with a decay of 0.00172% per cycle.

1. Introduction

Electrochemical energy storage systems have become promising substitutes for fossil fuels, wind energy, solar energy and tidal energy because of their attractive features of environmental friendliness, sustainability and quick response ability.^{1–5} Currently, supercapacitors and secondary batteries as two kinds of the most important energy storage systems greatly lead the energy application market, including portable electronic equipment, photovoltaic power systems and hybrid electric vehicles (HEVs).^{6–13} However, the low energy density of supercapacitors overly prevents their large-scale applications in long-range devices, while the low power density and short cycle lifetime of batteries also limit their developments in the high instantaneous power field. Given this, researchers attempt to integrate the advantages of supercapacitors and batteries into one device, called hybrid ion capacitors (HICs) based on lithium ions, sodium ions and potassium ions.^{6,13–19} However, the inflammability and toxicity of organic electrolytes are the toughest and trickiest issues that need to be solved in the future HICs. To overcome this problem, aqueous electrolytes have been widely investigated and used in HICs because of their high safety, fast ion conductivity and low manufacturing cost.^{20–22} Nevertheless, the narrow decomposition voltage of water (~ 1.23 V) leads to limited enhancement of energy density. Suo *et al.* employed a “water in salt” mixture with a wide voltage of 3 V as the electrolyte in lithium ion batteries, which can effectively improve the energy density.^{23–25} Meanwhile, Ji's group also had the aid of a “water in salt” electrolyte to construct high-voltage batteries.^{26–28} But the highly concentrated electrolytes often result in low ionic conductivity and high viscosity, which go against the improvement in rate capability and power density. In addition, the high ratio between the salt and water results in a high cost, especially for organic lithium salts.²⁹ As we all know, the redox potentials of water are closely associated with the pH value ($E_R = -0.0591\text{pH}$); specifically, the smaller the pH, the higher the oxygen evolution potential. In contrast, the larger the pH, the lower the hydrogen evolution potential.³⁰ Therefore,

^aJiangsu Key Laboratory of Electrochemical Energy Storage Technologies, College of Material Science and Engineering, Nanjing University of Aeronautics and Astronautics, Nanjing 210016, China. E-mail: azhangxg@nuaa.edu.cn

^bIntegrated Composites Laboratory, Department of Chemical and Biomolecular Engineering, University of Tennessee, Knoxville, TN 37996, USA. E-mail: zguo10@utk.edu

^cKey Laboratory of Materials Processing and Mold (Zhengzhou University), Ministry of Education, National Engineering Research Center for Advanced Polymer Processing Technology, Zhengzhou University, Zhengzhou, China

^dSchool of Materials Science and Engineering, North University of China, Taiyuan 030051, China

^eCollege of Materials Science and Engineering, Changsha University of Science and Technology, Changsha 410114, China

^fSchool of Urban Planning and Architecture, Southwest Minzu University, Chengdu 610041, China. E-mail: maixianmin@foxmail.com

† Electronic supplementary information (ESI) available: SEM images, XRD patterns, TG curves, CV and GCD curves, cycle stability, UV-vis spectrum, *etc.* See DOI: 10.1039/c9ta06734e

electrolytes with different pH values separated by functional separators have been widely explored to use in electrochemical energy storage devices. Hu *et al.* reported an aqueous electrochemical double-layer capacitor (EDLC) that exhibited a high energy density of 51 W h kg^{-1} more than 2 times that of previous reports.³¹ It needs to be emphasized that, in this system, asymmetric electrolytes with different pH were employed that not only benefited the redox reactions of the active additive, but also increased the cell voltage to 1.6 V. The design immensely shows a new attractive way to enhance the energy density of aqueous HICs.

In addition, most HICs are assembled by using inorganic battery materials and activated carbon (AC) as capacitive materials, for which the preparation process is complicated and power-wasting, and has high recovery cost.^{32–35} Compared with that, organic materials are promising candidates by virtue of their abundant sources, facile synthesis and biodegradability.^{36–39} Most importantly, the flexible structure of organic materials can broaden the selectivity of ion species and realize high rate capability, which extremely heightens their practical application possibility. The ingenious combination between organic materials and aqueous electrolyte makes metal-free, truly “green” energy storage devices possible. Polyimide has been investigated as a battery material in recent years because of its outstanding electrochemical performance in aqueous electrolyte such as high capacity, good rate capability and long cycle lifetimes.^{40,41} However, the capacitive material is the essential limiting factor in the improvement of the energy density of HICs because of the low capacitance, which usually gets less attention. Small dye molecules can produce a reversible redox reaction in the acidic electrolyte, and could be used as an electroactive additive in supercapacitors due to their dissolubility in aqueous electrolyte and satisfactory capacitance ($>300 \text{ F g}^{-1}$), higher than AC.^{42,43} However, the shuttle effect of the electroactive additive inevitably leads to serious self-discharging and poor coulombic efficiency. Kaner and co-workers attempted to rivet thionine on a graphene surface through π – π interactions.⁴⁴ The ideal combination makes the composite deliver 384 F g^{-1} at 1 A g^{-1} and excellent cycle stability. The only drawback is that the energy density and power density of the as-assembled device urgently need to be improved to satisfy the requirements for practical applications.

Herein, we successfully prepared methylene blue functionalized graphene composites with different mass ratios *via* a facile hydrothermal method. To confirm the structural composition of the as-prepared samples, various spectroscopies were employed. The results illustrated that the composites have high structural stability because of the extensive π -conjugated structure formed by the combination of the positively charged and readily available planar aromatic molecules and graphene. Additionally, enhanced electrochemical performances were obtained owing to the high electroactivity of MB and the good electronic conductivity of graphene, which have been verified by electrochemical impedance spectroscopy (EIS) analysis. Finally, novel aqueous HICs were designed and constructed by using polyimide (PI) as the anode and methylene blue (MB)

functionalized graphene as the cathode, and asymmetric solutions with different pH values as electrolytes. Linear sweep voltammetry (LSV) and charge–discharge measurements showed that HICs can operate well at a cell voltage of 1.9 V, higher than the decomposition voltage ($\sim 1.23 \text{ V}$) of water. Moreover, excellent performances including a maximum energy density of 48.6 W h kg^{-1} and a maximum power density of 19 kW kg^{-1} as well as a ultralong cycle lifetime were obtained (capacity retention of 82.8% after 10 000 cycles), making them a promising truly “green” energy storage system.

2. Experimental

2.1. Materials synthesis

2.1.1 Synthesis of 1,4,5,8-naphthalenetetracarboxylic dianhydride-derived polyimide (PI). Firstly, PI was prepared based on our previous reports.^{45,46} Specifically, equimolar 1,4,5,8-naphthalenetetracarboxylic dianhydride (NTCDA) easily reacted with ethylenediamine (EDA) in *N*-methylpyrrolidone (NMP) solvent for 8 h. After refluxing and filtering, the as-prepared product was dried and heated in a pure Ar atmosphere to remove the residual solvents, and then PI was yielded.

2.1.2 Preparation of methylene blue (MB) functionalized graphene. The GO dispersion (2 mg mL^{-1}) was purchased from the Carmery Materials Technology Co., Ltd. (Taiyuan, Shanxi) without further treatment. 40 mg of ascorbic acid (Vc) as a reducing-doping agent was added to 40 mL of GO dispersion and stirred vigorously for 30 min. Then, a certain quantity of MB was added to the above mixed solution and stirred continuously for 1 h. The mixture was transferred into a sealed Teflon-lined autoclave and kept at $180 \text{ }^\circ\text{C}$ for 10 h. After cooling to room temperature, the as-prepared samples were washed repeatedly with water and freeze-dried under vacuum. The final composites were marked as MB-*X* (*X* = the additive mass ratio of MB/(MB + GO) before the hydrothermal reaction). The rGO sample was prepared similarly to MB-*X*, but without the addition of MB.

2.2. Materials characterization

A field-emission scanning electron microscope (SEM, FESEM, HITACHI S-4800) was employed to observe the microscopic morphologies of samples. And EDS and element-mapping were carried out to confirm the elements in the as-prepared samples. The crystal structure was investigated with a Bruker D8 Advance X-ray diffractometer (XRD) using Cu $K\alpha$ radiation. X-ray photoelectron spectroscopy (XPS) was performed on a PerkinElmer PHI 550 spectrometer with Al $K\alpha$ (1486.6 eV). Fourier transform infrared (FT-IR) spectra were collected on a Shimadzu IR Prestige-21 FT-IR spectrometer with KBr pellets. Ultraviolet-visible (UV-vis) spectroscopy was performed on a UV-1102 spectrophotometer. Raman spectra were recorded using a HORIBA Scientific LabRAM HR Raman spectrometer. To estimate the contents of water and MB, thermogravimetric (TG) analysis was performed from 30 to $600 \text{ }^\circ\text{C}$ using a PerkinElmer TG/DTG-6300, with a heating rate of $5 \text{ }^\circ\text{C min}^{-1}$ in air atmosphere.

2.3. Electrochemical measurements

The PI anode was prepared by pressing the film containing PI, acetylene black and polytetrafluoroethylene (PTFE) with a mass ratio of 6 : 3 : 1 on Ti mesh. MB-based cathodes were fabricated by pressing the film containing active materials, acetylene black and PTFE in a mass ratio of 8 : 1 : 1 on Ti mesh. The active mass loading on all electrodes was 2 mg. The electrochemical performances of individual electrodes were investigated by using Swagelok™ T-cells, where the excess active carbon film and saturated calomel electrode (SCE) acted as the counter electrode and reference electrode, respectively, and 1 M (NH₄)₂SO₄ and 1 M H₂SO₄ served as the electrolyte for the anode and cathode, respectively. Aqueous HICs were designed and assembled, in which PI acted as the anode and MB-45 served as the cathode with an active mass ratio of 1 : 1.5 (2 mg : 3 mg), and asymmetric electrolytes were separated by an anion-exchange membrane. Cyclic voltammetry (CV) and galvanostatic charge–discharge (GCD) curves were recorded on a CHI 760e electrochemical workstation for both three-electrode systems and HICs. Cycle performance was tested with a CT20001A cell test instrument (LAND Electronic Co.). EIS measurements were performed using an electrochemical workstation (Zive SP2, WonATech) with frequencies ranging from 0.01 to 100 kHz. The specific capacitance (C , F g⁻¹) can be calculated based on the following equation:

$$C = \frac{i \times t}{\Delta V \times m} \quad (1)$$

where i (A) is the current density, t (s) is the discharge time, ΔV (V) is the working voltage, and m (g) is the mass loading of active materials.

In addition, the specific energy density (E , W h kg⁻¹) and power density (P , W kg⁻¹) are estimated by the following formulas:

$$E = \int_{t_1}^{t_2} i \Delta V dt \quad (2)$$

$$P = \frac{3600E}{\Delta t} \quad (3)$$

where t_1 and t_2 are the start/end-of-discharge time of the SIC, and Δt is the difference value of t_2 and t_1 .

3. Results and discussion

The microscopic morphologies of samples were analyzed using SEM, and are shown in Fig. 1a and S1a–d.† It is clear to see that rGO still retains its nanosheet morphology without severe aggregation after functionalizing by MB, even after increasing the content of MB up to 60%. XRD patterns of rGO, MB and MB-45 are presented in Fig. S2.† In the XRD pattern of rGO, there are two main diffraction peaks at around of 25° and 45°, corresponding to the (002) and (100) planes of graphitic carbon, respectively.⁴⁷ As displayed from the pattern of MB-45, the co-existence of characteristic diffraction peaks of rGO and MB illustrates that MB is successfully fixed on the rGO surface. The weakening of MB characteristic diffraction peaks is principally

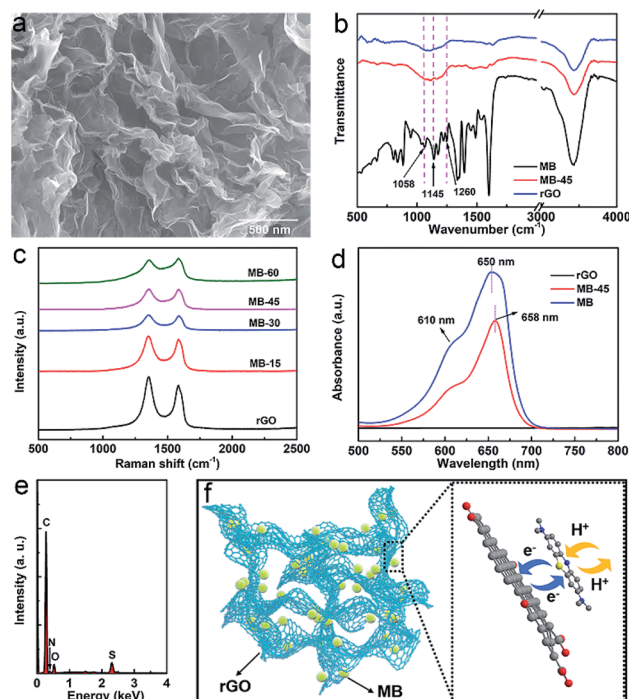


Fig. 1 (a) SEM image of MB-45, (b) FT-IR spectra of MB, rGO and MB-45, (c) Raman spectra of samples with different contents, (d) UV absorption spectra of MB, rGO and MB-45. (e) EDS spectrum of MB-45, and (f) schematic illustration of MB-X (left part) and its energy storage mechanism (right part).

related to the content of MB in the composite. As shown in Fig. S3,† TG curve comparison of rGO and MB-45 illustrates that the real mass ratio of MB in the MB-45 composite is 34.6% smaller than the initial amount.

FT-IR spectra were obtained to estimate the chemical composition of the samples, as shown in Fig. 1b. Compared to the spectrum of pure rGO, that of MB-45 displays two extra peaks at about 1058 and 1145 cm⁻¹ that can be attributed to the C–S bending vibrations in the heteroaromatic ring of the MB. Compared with that of pure MB, a slight low wavenumber shift in the bands is observed for MB-45 that is likely the effect of the π network.⁴⁸ Additionally, the absence of the characteristic stretching vibrational bands of C–N in amide groups at \approx 1260 cm⁻¹ illustrates a covalent conjugation, which is in accordance with previous reports.^{44,49,50} Raman spectroscopy can be used to investigate the surface properties of samples. As seen from Fig. 1c, there are two peaks in all Raman spectra, that is, the D band and G band. The D band represents the defects or the sp³ hybridized carbon atoms at the edges on the graphene basal plane, while the G band stands for the stretching vibration of any pair of sp² sites in the hexagonal carbon framework.^{51,52} Distinctly, with the increased mass ratio of MB in samples, the values of I_D/I_G gradually decrease, which is indicative of decreasing defects and disorders because of the extensive π -conjugated structure formed by the combination of the positively charged and readily available planar aromatic molecules and graphene. Fig. 1d shows the UV absorption spectra of MB,

rGO and MB-45. There is no peak observed in the UV spectrum of rGO within the wavelength range from 500 to 800 nm. The absorption peak at 650 nm in the UV spectrum of MB belongs to the $n \rightarrow \pi^*$ transition of C=N bonds of MB in its monomeric form.⁵³ And the shoulder peak at 610 nm can be derived from dimer aggregation.⁵⁴ In terms of the UV spectrum of MB-45, all peaks ascribed to MB still exist along with a red shift (about 8 nm) based on the $n \rightarrow \pi^*$ transition of the C=N bonds of MB, confirming the presence of delocalized π -electrons in the conjugated MB-45 composite, namely, π - π stacking interaction.⁴⁸ EDS mappings demonstrate that the composites mainly contain C, O, N and S elements, where O is attributed to the defects on rGO surface, and N and S belong to MB molecules, respectively, as shown in Fig. 1e. The element-mappings clearly show a uniform distribution (Fig. S1e-h†). Fig. 1f illustrates the formation process of MB-X and its energy storage mechanism (right part). During the hydrothermal reaction, GO is reduced to rGO, and MB with a positive charge and the available planar aromatic structure are easily riveted on the rGO surface to form conjugated macromolecules through electrostatic and extensive π -conjugated interaction. In the charge/discharge process, rGO as a good electron carrier results in an outstanding rate capability, and MB as the electroactive material plays a key role in the enhancement of capacitance.

XPS was performed to further confirm the composition of the samples. Fig. 2a shows the overall XPS spectra of rGO, MB and MB-45. It is clear from the XPS spectrum that only C and O elements are present in rGO, while O, S and N elements exist in that of MB. Notably, the O element found in MB is ascribed to crystal water. In the XPS spectrum of MB, all the elements mentioned above are observed, illustrating successful synthesis of MB-45. In detail, the XPS spectrum of the C 1s of MB-45 reveals two main peaks that can be fitted into six peaks (Fig. 2b). Among them, the peak at 285.8 eV is ascribed to C-N/C-S bonds in MB molecules. Fig. 2c shows the deconvoluted core level XPS spectrum of N 1s, in which two peaks located at 399 and 400 eV

are attributed to C=N and C-N, respectively.⁵⁵ In addition, the S 2p spectrum includes two peaks at 164.1 and 165.3 eV corresponding to C-S and C=S, respectively, as presented in Fig. 2d. The above results also confirm successful non-covalent functionalization of rGO by MB molecules.

The electrochemical performances of all samples were investigated by using a three-electrode system in 1 M H₂SO₄ electrolyte, including CV, GCD and EIS tests. Fig. 3a and S4a-d† show CV curves of rGO and MB-X at different scan rates. It is obvious to see that all CV curves display a pair of redox peaks, which is attributed to the redox of MB anchored on the graphene surface except that of rGO resulted from oxygen-containing groups. Meanwhile, for all CV curves, the potential differences slightly increase and remain well symmetrical with the increasing scan rates, illustrating good redox reversibility and high electrochemical activity. As shown in the GCD curves at various current densities of MB-X (Fig. 3b and 5a-d), the obvious platforms found in all curves correspond to the redox peaks in CV curves. As for MB-45, a specific capacitance of 317.7 F g⁻¹ is obtained at 0.5 A g⁻¹ and up to 261.5 F g⁻¹ can be retained even at a high current density of 20 A g⁻¹, indicative of the excellent rate capability. The expected result is mainly ascribed to the synergistic effect between graphene and MB: (a) the high conductivity of graphene that realizes fast electron transport; (b) MB has a flexible structure benefiting its combination with H⁺, making the composites ideal capacitive materials. The reaction mechanism of MB molecules in acidic electrolyte is displayed in Fig. 3c; the reaction involving H⁺ corresponds to a couple of redox peaks shown in CV curves and platforms displayed in GCD curves.

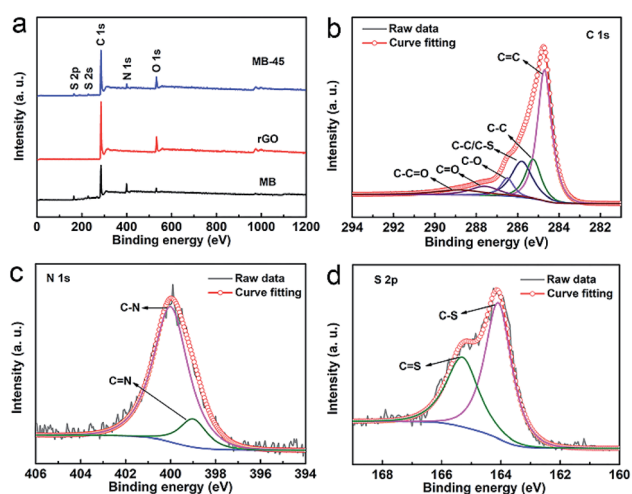


Fig. 2 (a) Overall XPS spectra of rGO, MB and MB-45, and deconvoluted core level XPS spectra of MB-45 (b) C 1s, (c) N 1s and (d) S 2p, respectively.

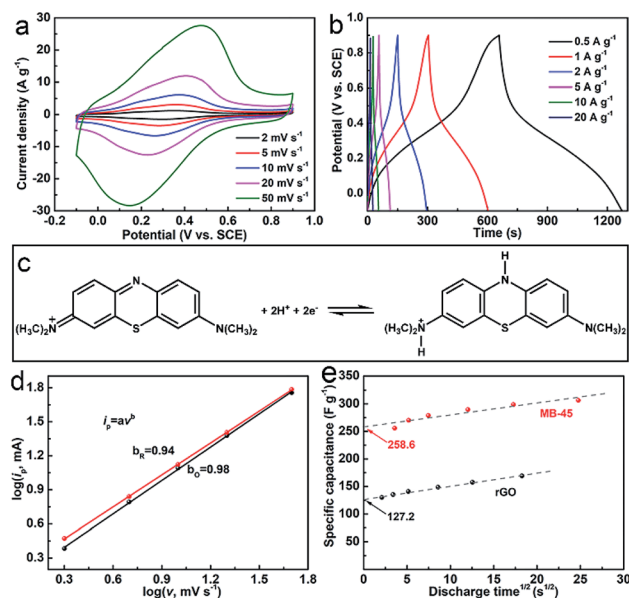


Fig. 3 (a) CV curves of MB-45 at different scan rates, (b) GCD profiles of MB-45 at various current densities, (c) reaction mechanism for MB molecules in acidic electrolyte, (d) the relationships between $\log i_p$ and $\log v$ based on peak currents, and (e) capacity versus square root of half-charge/discharge time. Extrapolated intercept capacitance is rate-independent capacitance k_1 , the remainder diffusion-controlled capacitance.

The kinetic process of MB-X is inspected based on the relationship between $\log i_p$ and $\log v$, where i_p stands for the peak current and v is the scan rate, as shown in Fig. 3d and S6a–c.† After fitting, the slopes of the lines based on reduction and oxidation are both greater than 0.9, which are close to 1, showing that the electrochemical process of MB-X is not controlled by diffusion, but the surface redox reaction. As we know, the capacitance C may consist of a rate-independent component k_1 (typically attributed to EDLC) and a diffusion limited component k_2 controlled by the charge/discharge time (t), as shown in the following formula:^{56–58}

$$C = k_1 + k_2 t^{1/2}$$

As shown in Fig. 3e, k_1 can be obtained by the extrapolation at the $t^{1/2} = 0$ intercept with values of 258.6 and 127.2 F g⁻¹, holding about 81.4 and 75.1% of the total capacitances for MB-45 and rGO, respectively. And the rate-independent component proportions at different discharge time closely related to current density are shown in Fig. S7,† obviously, the capacitive contribution increases with increasing current density. This result could be due to the fact that MB molecules are parallel to the sp² network of the graphene by π - π interaction without destruction of their conjugated structure, so the composite can deliver an EDLC-like charge transfer reaction in redox reactions. The cycle performance of MB-45 at 5 A g⁻¹ is shown in Fig. S8a.† After cycling for 3000 cycles, charge and discharge capacitance retentions are both more than 90% accompanied by a high coulombic efficiency beyond 98%, implying a good reversible reaction. As shown in Fig. S8b,† compared with the UV spectrum of 5 mM MB in 1 M H₂SO₄, that of the electrolyte after 3000 cycles displays analogous absorption peaks but ultralow absorbance, illustrating an outstanding stability resulting from a strong π - π interaction between MB molecules and graphene.

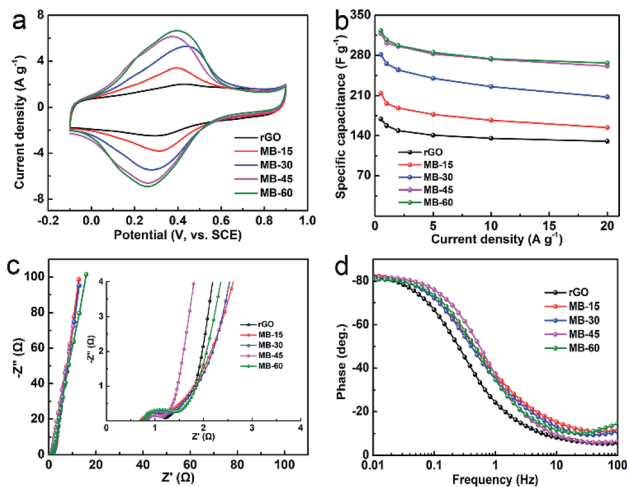


Fig. 4 Electrochemical performances of samples. (a) CV curves at 10 mV s⁻¹ and (b) specific capacitance at different current densities of rGO and MB-X, (c) EIS spectra with a magnified high-frequency region as an inset and (d) Bode plots of phase angle versus frequency for rGO and MB-X.

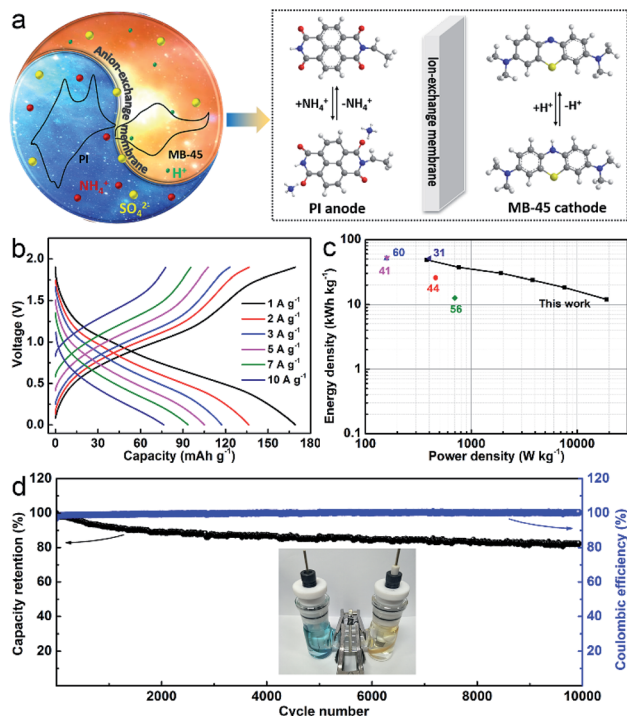


Fig. 5 (a) Schematic diagram of HICs with asymmetric electrolytes and energy storage mechanisms (right part), (b) GCD plots of HICs at different current densities, (c) Ragone plot of the assembled PI//MB-45 HICs, and (d) cycle performance at 5 A g⁻¹ and coulombic efficiency of PI//MB-45 HICs and digital photograph of HICs based on H-type cells (inset).

Fig. 4a shows the CV curves of all samples at 10 mV s⁻¹. Obviously, current densities linearly vary with the increasing MB content, meaning an enhancement of capacitance. Fig. 4b plots the relationship of current density and specific capacitance of all samples. Compared to pure rGO, the capacitances are drastically improved from 169 to 323 F g⁻¹ in MB-X samples. Meanwhile, MB-45 and MB-60 are comparable in capacitance, because of the saturated adsorption extent of MB on the graphene sheet surface. EIS was performed to investigate the charge and ion transport properties of MB-X samples. As shown in Fig. 4c, all samples display small equivalent series resistance. But in the magnified view of the high-frequency region (inset). We can see that MB-45 exhibits the smallest charge transfer resistance compared to others, signifying the best kinetic process. Fig. 4d shows the phase-angle plots of MB-X samples. The phase angles of all samples are about -80°, which are close to the -90° for ideal capacitors.⁵⁹ The time constants τ_0 ($\tau_0 = 1/f_0$) obtained from the Bode plot at a phase angle of -45° at 0.31, 0.61, 0.53, 0.69 and 0.58 Hz are 3.22, 1.63, 1.88, 1.44 and 1.72 s for rGO, MB-15, MB-30, MB-45 and MB-60, respectively. The smaller value of MB-X than that of rGO implies a high electroactivity of MB. Additionally, the shortest time constant of MB-45 indicates the fastest response time among all samples. According to the above results, MB-45 as the best sample is chosen to investigate the following studies.

The PI polymer was used as the anode material in 1 M $(\text{NH}_4)_2\text{SO}_4$ electrolyte to construct HICs because of the good rate capability and excellent cycle stability resulting from the flexible structure of PI and the small size of hydrated NH_4^+ .⁶⁰ The electrochemical performance is shown in Fig. S9a and b.† Based on the good electrochemical performances of both the MB-45 cathode and PI anode, HIC is successfully constructed, as shown in Fig. 5a. The specific energy storage mechanism is vividly demonstrated in the right part, where the PI anode and MB based cathode react with NH_4^+ and H^+ , respectively, and SO_4^{2-} ions act as charge carriers to balance charge in the charge/discharge process with the aid of an anion-exchange membrane. Fig. S10a† shows the LSV curve of the asymmetric electrolytes based on Ti mesh without active materials. We can see that the current response with a potential ranging from -1.0 to 1.0 V is much smaller than those of the PI anode and MB-45 cathode (Fig. S10b†), which signifies little or no water decomposition. Meanwhile, the larger potential range can adequately contain the redox potentials of the MB-45 cathode and PI anode. The maximum cell voltage of the as-assembled HIC can be obtained based on the highest potential of the cathode and the lowest potential of the anode within 1.9 V, as shown in Fig. S10c.† Fig. 5b shows the GCD curves of HICs at different current densities. A high capacity of $169.2 \text{ mA h g}^{-1}$ at 1 A g^{-1} is obtained based on the mass of PI anode materials (2 mg), and 76.3 mA h g^{-1} at 10 A g^{-1} is well retained, showing an outstanding rate capability. Fig. S10d† displays the EIS spectrum of HIC. The series resistance (R_s) and charge transfer resistance (R_{ct}) are estimated to be 1.074 and 19.87 Ω , respectively, which are smaller than those of organic HICs, illustrating high ionic conductivity and diffusion. As displayed in the Ragone plot of the SIC (Fig. 5c), we can find a maximum energy density of 48.6 W h kg^{-1} and a maximum power density of 19 kW kg^{-1} based on the total active mass of both the cathode and anode, which is comparable to those of a PI//PTMA aqueous battery,⁶⁰ “water in salt” electrolyte based PI//PTPA battery,⁴¹ and AC//AC supercapacitor with a TEMOP additive in asymmetric electrolytes,³¹ and superior to those of thionine//graphene aerogel⁴⁴ and danthron/graphene based symmetric devices.⁵⁶

Certainly, a good HIC should have a long cycle lifetime. As presented in Fig. 5d, the as-fabricated HIC can operate well with ultralong cycles even after 10 000 cycles (capacity retention of 82.8%). The attractive cycle performance is mainly due to the flexible structure of the organic electrode materials and low solubility of polymer materials in aqueous electrolyte as well as the strong π - π interaction between MB molecules and graphene. In addition, the inset in Fig. 5d shows the digital photograph of HICs based on H-type cells, where asymmetric electrolytes with different pH values can be roughly detected by using test strips. We can see that electrolytes in the cathode and anode still reveal different colours after 200 cycles, manifesting practical applicability of the anion-exchange membrane. The above results make our HICs have extensive application prospects and facilitate the implementation of truly “green” energy storage devices.

4. Conclusions

In summary, we have successfully prepared methylene blue functionalized graphene composites with a facile hydrothermal method. The MB-45 composite delivers outstanding electrochemical performance such as high capacitance, good capability and long cycle lifetimes, which can be attributed to the strong π - π interaction and electrostatic interaction between MB molecules and graphene. Additionally, a novel aqueous HIC with a larger cell voltage of 1.9 V is designed and constructed based on asymmetric electrolytes. Thanks to organic electrode materials with a flexible structure and high electrochemical activity, the as-fabricated HIC exhibits a maximum energy density of 48.6 W h kg^{-1} and a maximum power density of 19 kW kg^{-1} , as well as an ultralong cycle lifetime (82.8% capacity retention after 10 000 cycles). This ingenious design can provide an efficient way to construct high-performance HICs and realize truly “green” energy storage systems.

Conflicts of interest

There are no conflicts to declare.

Acknowledgements

This work was supported by the National Natural Science Foundation of China (no. U1802256, 51372116, 51672128, 51802154, 21773118 and 21875107), the Natural Science Foundation of Jiangsu Province (no. BK20170778), the Key Research and Development Program in Jiangsu Province (BE2018122), the Nanjing University of Aeronautics and Astronautics PhD short-term visiting scholar project (no. 190106DF06), the Post-graduate Research & Practice Innovation Program of Jiangsu Province (KYCX18_0279) and a Project Funded by the Priority Academic Program Development of Jiangsu Higher Education Institutions (PAPD).

References

- (a) X. Yu and A. Manthiram, *Joule*, 2017, **1**, 453–462; (b) R. Nie, Q. Wang, P. Sun, R. Wang, Q. Yuan and X. Wang, *Eng. Sci.*, 2019, **6**, 22–29, DOI: 10.30919/es8d668; (c) F. Li, Z. Wei, A. Manthiram, *et al.*, *J. Mater. Chem. A*, 2019, **7**, 9406–9431; (d) J. Zhang, Z. Zhang, Y. Jiao, H. Yang, Y. Li, J. Zhang and P. Gao, *J. Power Sources*, 2019, **419**, 99–105; (e) J. Ren, Q. Luo, Q. Hou, H. Chen, *et al.*, *ChemElectroChem*, 2019, **6**, 3167–3174; (f) K. Sun, R. Fan, X. Zhang, *et al.*, *J. Mater. Chem. C*, 2018, **6**, 2925–2943.
- (a) Y. Wang, Y. Song and Y. Xia, *Chem. Soc. Rev.*, 2016, **45**, 5925–5950; (b) M. Liu, Y. Liu, Y. Yan, F. Wang, J. Liu and T. Liu, *Chem. Commun.*, 2017, **53**, 9097–9100; (c) X. Xie, M. Mao, S. Qi and J. Ma, *CrystEngComm*, 2019, **21**, 3755–3769; (d) R. Li, X. Zhu, Q. Fu, *et al.*, *Chem. Commun.*, 2019, **55**, 2493–2496; (e) J. Liao, R. Tan, Z. Kuang, *et al.*, *Chin. Chem. Lett.*, 2018, **29**, 1785–1790; (f) Q. Hou, J. Ren, H. Chen, *et al.*, *ChemElectroChem*, 2018, **5**, 726–731.

- 3 (a) B. E. Conway, *J. Electrochem. Soc.*, 1991, **138**, 1539–1548; (b) S. Qi, X. Xie, X. Peng, *et al.*, *Phys. Status Solidi RRL*, 2019, 1900209; (c) M. Idrees, S. Batool, J. Kong, *et al.*, *Electrochim. Acta*, 2019, **296**, 925–937; (d) M. Liu, Z. Yang, H. Sun, C. Lai, X. Zhao, H. Peng and T. Liu, *Nano Res.*, 2016, **9**, 3735–3746; (e) M. Idrees, S. Batool, Q. Zhuang, *et al.*, *Ceram. Int.*, 2019, **45**, 10572–10580.
- 4 (a) D. Tie, S. Huang, J. Wang, Y. Zhao, J. Ma and J. Zhang, *Energy Storage Mater.*, 2019, DOI: 10.1016/j.ensm.2018.12.018; (b) Y. Zhai, J. Wang, Q. Gao, Y. Fan, C. Hou, Y. Hou, H. Liu, Q. Shao, S. Wu, L. Zhao, T. Ding, F. Dang and Z. Guo, *J. Catal.*, 2019, DOI: 10.1016/j.jcat.2019.07.055.
- 5 (a) M. Wu, W. Ni, J. Hu and J. Ma, *Nano-Micro Lett.*, 2019, **11**, 44; (b) W. Zhao, X. Li, R. Yin, *et al.*, *Nanoscale*, 2019, **11**, 50–59; (c) J. Tian, Q. Shao, X. Dong, *et al.*, *Electrochim. Acta*, 2018, **261**, 236–245; (d) X. Lou, C. Lin, Q. Luo, *et al.*, *ChemElectroChem*, 2017, **4**, 3171–3180; (e) H. Borate, A. Rokade, S. Pandharkar, *et al.*, *ES Materials & Manufacturing*, 2019, **3**, 22–28, DOI: 10.30919/esmm5f202.
- 6 (a) W. Zuo, R. Li, C. Zhou, Y. Li, J. Xia and J. Liu, *Adv. Sci.*, 2017, **4**, 1600539; (b) K. Le, Z. Wang, F. Wang, *et al.*, *Dalton Trans.*, 2019, **48**, 5193–5202; (c) Y. Ma, C. Hou, H. Zhang, *et al.*, *Electrochim. Acta*, 2019, **315**, 114–123; (d) W. Du, X. Wang, J. Zhan, *et al.*, *Electrochim. Acta*, 2019, **296**, 907–915; (e) B. Xu, S. Qi, P. He and J. Ma, *Chem.–Asian J.*, 2019, DOI: 10.1002/asia.201900784; (f) C. Lin, H. Hu, C. Cheng, *et al.*, *Electrochim. Acta*, 2018, **260**, 65–72.
- 7 (a) B. Li, J. Zheng, H. Zhang, L. Jin, D. Yang, H. Lv, C. Shen, A. Shellikeri, Y. Zheng, R. Gong, J. P. Zheng and C. Zhang, *Adv. Mater.*, 2018, **30**, e1705670; (b) B. Kirubasanakar, V. Murugadoss, J. Lin, *et al.*, *Nanoscale*, 2018, **10**, 20414–20425; (c) W. Deng, T. Kang, H. Liu, *et al.*, *Sci. Adv. Mater.*, 2018, **10**, 937–949.
- 8 (a) J. Jiang, Y. Zhang, P. Nie, G. Xu, M. Shi, J. Wang, Y. Wu, R. Fu, H. Dou and X. Zhang, *Adv. Sustainable Syst.*, 2018, **2**, 1700110; (b) C. Cui, H. Wang, M. Wang, *et al.*, *Small*, 2019, **26**, e1902659.
- 9 M. R. Lukatskaya, B. Dunn and Y. Gogotsi, *Nat. Commun.*, 2016, **7**, 12647–12659.
- 10 (a) C. Hou, Z. Tai, L. Zhao, Y. Zhai, Y. Hou, Y. Fan, F. Dang, J. Wang and H. Liu, *J. Mater. Chem. A*, 2018, **6**, 9723–9736; (b) Y. Liu, M. Shi, C. Yan, *et al.*, *J. Mater. Sci.*, 2019, **30**(7), 6583–6592; (c) L. Yang, M. Shi, J. Jiang, *et al.*, *Mater. Lett.*, 2019, **244**, 27–30.
- 11 M. Wang, Y. Zhao, X. Zhang, R. Qi, S. Shi, Z. Li, Q. Wang and Y. Zhao, *Electrochim. Acta*, 2018, **272**, 184–191.
- 12 (a) C. Hou, Y. Hou, Y. Fan, Y. Zhai, Y. Wang, Z. Sun, R. Fan, F. Dang and J. Wang, *J. Mater. Chem. A*, 2018, **6**, 6967–6976; (b) M. Liu, B. Li, H. Zhou, C. Chen, Y. Liu and T. Liu, *Chem. Commun.*, 2017, **53**, 2810–2813; (c) M. Liu, Q. Meng, Z. Yang, X. Zhao and T. Liu, *Chem. Commun.*, 2018, **54**, 5090–5093; (d) H. Dong, Y. Li, H. Chai, Y. Cao and X. Chen, *ES Energy & Environment*, 2019, **4**, 19–26, DOI: 10.30919/eseec2c21.
- 13 L. Wang, X. Xie, K. Dinh, Q. Yan and J. Ma, *Coord. Chem. Rev.*, 2019, **397**, 138–167.
- 14 H. Wang, Y. Zhang, H. Ang, Y. Zhang, H. T. Tan, Y. Zhang, Y. Guo, J. B. Franklin, X. L. Wu, M. Srinivasan, H. J. Fan and Q. Yan, *Adv. Funct. Mater.*, 2016, **26**, 3082–3093.
- 15 J. Jiang, P. Nie, B. Ding, Y. Zhang, G. Xu, L. Wu, H. Dou and X. Zhang, *J. Mater. Chem. A*, 2017, **5**, 23283–23291.
- 16 Y. Zhang, P. Nie, C. Xu, G. Xu, B. Ding, H. Dou and X. Zhang, *Electrochim. Acta*, 2018, **268**, 512–519.
- 17 M. Wang, F. Jin, X. Zhang, J. Wang, S. Huang, X. Zhang, S. Mu, Y. Zhao and Y. Zhao, *ACS Sustainable Chem. Eng.*, 2017, **5**, 5679–5685.
- 18 J. Ding, H. Wang, Z. Li, K. Cui, D. Karpuzov, X. Tan, A. Kohandehghan and D. Mitlin, *Energy Environ. Sci.*, 2015, **8**, 941–955.
- 19 H. V. Ramasamy, B. Senthilkumar, P. Barpanda and Y.-S. Lee, *Chem. Eng. J.*, 2019, **368**, 235–243.
- 20 H. Kim, J. Hong, K. Y. Park, H. Kim, S. W. Kim and K. Kang, *Chem. Rev.*, 2014, **114**, 11788–11827.
- 21 J. Huang, Z. Guo, Y. Ma, D. Bin, Y. Wang and Y. Xia, *Small Methods*, 2019, **3**, 1800272.
- 22 Y. Zhang, Z. Hu, Y. Liang, Y. Yang, N. An, Z. Li and H. Wu, *J. Mater. Chem. A*, 2015, **3**, 15057–15067.
- 23 K. Xu and C. Wang, *Nat. Energy*, 2016, **1**, 16161–16162.
- 24 L. Suo, O. Borodin, T. Gao, M. Olguin, J. Ho, X. Fan, C. Luo, C. Wang and K. Xu, *Science*, 2015, **350**, 938–943.
- 25 L. Suo, F. Han, X. Fan, H. Liu, K. Xu and C. Wang, *J. Mater. Chem. A*, 2016, **4**, 6639–6644.
- 26 D. P. Leonard, Z. Wei, G. Chen, F. Du and X. Ji, *ACS Energy Lett.*, 2018, **3**, 373–374.
- 27 X. Wu, Y. Xu, C. Zhang, D. P. Leonard, A. Markir, J. Lu and X. Ji, *J. Am. Chem. Soc.*, 2019, **141**, 6338–6344.
- 28 J. J. Holoubek, H. Jiang, D. Leonard, Y. Qi, G. C. Bustamante and X. Ji, *Chem. Commun.*, 2018, **54**, 9805–9808.
- 29 X. Bu, L. Su, Q. Dou, S. Lei and X. Yan, *J. Mater. Chem. A*, 2019, **7**, 7541–7547.
- 30 G. Economy, R. Speiser, F. Beck and M. Fontana, *J. Electrochem. Soc.*, 1961, **108**, 337–343.
- 31 L. Hu, C. Shi, K. Guo, T. Zhai, H. Li and Y. Wang, *Angew. Chem.*, 2018, **57**, 8214–8218.
- 32 F. Li, Z. Wei, A. Manthiram, Y. Feng, J. Ma and L. Mai, *J. Mater. Chem. A*, 2019, **7**, 9406–9431.
- 33 K. Chayambuka, G. Mulder, D. L. Danilov and P. H. L. Notten, *Adv. Energy Mater.*, 2018, **8**, 1800079.
- 34 V. Aravindan, J. Gnanaraj, Y.-S. Lee and S. Madhavi, *Chem. Rev.*, 2014, **114**, 11619–11635.
- 35 X. Xie, M. Mao, S. Qia and J. Ma, *CrystEngComm*, 2019, **21**, 3755–3769.
- 36 Z. Song and H. Zhou, *Energy Environ. Sci.*, 2013, **6**, 2280–2301.
- 37 Q. Zhao, Y. Lu and J. Chen, *Adv. Energy Mater.*, 2017, **7**, 1601792.
- 38 S. Lee, G. Kwon, K. Ku, K. Yoon, S. K. Jung, H. D. Lim and K. Kang, *Adv. Mater.*, 2018, **30**, e1704682.
- 39 C. Hou, J. Wang, W. Du, J. Wang, Y. Du, C. Liu, J. Zhang, H. Hou, F. Dang, L. Zhao and Z. Guo, *J. Mater. Chem. A*, 2019, **7**, 13460–13472.
- 40 Z. Guo, L. Chen, Y. Wang, C. Wang and Y. Xia, *ACS Sustainable Chem. Eng.*, 2017, **5**, 1503–1508.

- 41 X. Dong, H. Yu, Y. Ma, J. L. Bao, D. G. Truhlar, Y. Wang and Y. Xia, *Chemistry*, 2017, **23**, 2560–2565.
- 42 X. Ren, Z. Hu, H. Hu, R. Qiang, L. Li, Z. Li, Y. Yang, Z. Zhang and H. Wu, *Mater. Res. Bull.*, 2015, **70**, 215–221.
- 43 S. Roldán, M. Granda, R. Menéndez, R. Santamaría and C. Blanco, *Electrochim. Acta*, 2012, **83**, 241–246.
- 44 Y. Shabangoli, M. S. Rahmanifar, M. F. El-Kady, A. Noori, M. F. Mousavi and R. B. Kaner, *Adv. Energy Mater.*, 2018, **8**, 1802869.
- 45 Y. Zhang, Y. An, J. Jiang, S. Dong, L. Wu, R. Fu, H. Dou and X. Zhang, *Energy Technol.*, 2018, **6**, 2146–2153.
- 46 Y. Zhang, Y. An, S. Dong, J. Jiang, H. Dou and X. Zhang, *J. Phys. Chem. C*, 2018, **122**, 22294–22300.
- 47 J. Zhao, Y.-Z. Zhang, F. Zhang, H. Liang, F. Ming, H. N. Alshareef and Z. Gao, *Adv. Energy Mater.*, 2019, **9**, 1803215.
- 48 N. An, Y. An, Z. Hu, B. Guo, Y. Yang and Z. Lei, *J. Mater. Chem. A*, 2015, **3**, 22239–22246.
- 49 E. Krzyszkowska, J. Walkowiak-Kulikowska, S. Stienen and A. Wojcik, *Phys. Chem. Chem. Phys.*, 2017, **19**, 14412–14423.
- 50 D. Zhang, L. Fu, L. Liao, B. Dai, R. Zou and C. Zhang, *Electrochim. Acta*, 2012, **75**, 71–79.
- 51 X. Wang, Y. Yang, Q. Zhang, X. Yang and Z. Hu, *J. Phys. Chem. C*, 2018, **122**, 6526–6538.
- 52 M. Wojtoniszak, D. Rogińska, B. Machaliński, M. Drozdziak and E. Mijowska, *Mater. Res. Bull.*, 2013, **48**, 2636–2639.
- 53 T. Y. Zhang, T. Oyama, A. Aoshima, H. Hidaka, J. C. Zhao and N. Serpone, *J. Photochem. Photobiol., A*, 2001, **140**, 163–172.
- 54 S. Jockusch, N. J. Turro and D. A. Tomalia, *Macromolecules*, 1995, **28**, 7416–7418.
- 55 J.-L. Gong, Y.-L. Zhang, Y. Jiang, G.-M. Zeng, Z.-H. Cui, K. Liu, C.-H. Deng, Q.-Y. Niu, J.-H. Deng and S.-Y. Huan, *Appl. Surf. Sci.*, 2015, **330**, 148–157.
- 56 N. An, Z. Hu, H. Wu, Y. Yang, Z. Lei and W. Dong, *J. Mater. Chem. A*, 2017, **5**, 25420–25430.
- 57 T. Q. Lin, I. W. Chen, F. X. Liu, C. Y. Yang, H. Bi, F. F. Xu and F. Q. Huang, *Science*, 2015, **350**, 1508–1513.
- 58 V. Augustyn, J. Come, M. A. Lowe, J. W. Kim, P. L. Taberna, S. H. Tolbert, H. D. Abruna, P. Simon and B. Dunn, *Nat. Mater.*, 2013, **12**, 518–522.
- 59 J. Wang, J. Tang, B. Ding, Z. Chang, X. Hao, T. Takei, N. Kobayashi, Y. Bando, X. Zhang and Y. Yamauchi, *Small*, 2018, **14**, e1704461.
- 60 Y. Zhang, Y. An, B. Yin, J. Jiang, S. Dong, H. Dou and X. Zhang, *J. Mater. Chem. A*, 2019, **7**, 11314–11320.